

Hubble Space Telescope STIS Observations of the Accreting White Dwarfs in BW Scl, BC UMa and SW UMa¹

Boris T. Gänsicke

Department of Physics, University of Warwick, Coventry CV4 9BU

`Boris.Gaensicke@warwick.ac.uk`

Paula Szkody

Astronomy Department, University of Washington, Seattle, WA 98195

`szkody@astro.washington.edu`

Steve B. Howell

WIYN Observatory & NOAO, 950 N. Cherry Avenue, Tucson, AZ 85726

`howell@noao.edu`

Edward M. Sion

Department of Astronomy and Astrophysics, Villanova University, Villanova, PA 19085

`Edward.Sion@villanova.edu`

ABSTRACT

We have observed the short-period dwarf novae BW Scl, BC UMa and SW UMa using the *Hubble Space Telescope*/Space Telescope Imaging Spectrograph. In all three systems, the white dwarf is the dominant source of far-ultraviolet flux, even though in BC UMa and SW UMa an additional continuum component contributes $\sim 10\%$ and $\sim 20\%$ of the 1400 \AA flux, respectively. Fitting the data with detailed white dwarf model spectra, we determine the effective temperatures to be $14\,800 \pm 900\text{ K}$ (BW Scl), $15\,200 \pm 1000\text{ K}$ (BC UMa), and

¹Based on observations made with the NASA/ESA Hubble Space Telescope obtained at the Space Telescope Science Institute which is operated by the AURA under NASA contract NAS 5-26555 and with the Apache Point Observatory (APO) 3.5-m telescope which is operated by the Astrophysical Research Consortium (ARC).

13 900 ± 900 K (SW UMa). The additional continuum component in BC UMa and SW UMa is equally well described by either a blackbody or a power law, which could be associated with emission from the hot spot or from an optically thin accretion disk (or an optically thin layer on top of a colder optically thick disk), respectively. Modelling the narrow metal lines detected in the STIS spectra results in sub-solar abundances of carbon, oxygen and silicon for all three systems, and also suggests substantial supra-solar abundances of aluminium. The narrow absorption line profiles imply low white dwarf rotation rates, $v \sin i \lesssim 300 \text{ km s}^{-1}$ for the three white dwarfs. SW UMa is the only system that shows significant short-term variability in the far-ultraviolet range, which is primarily associated with the observed emission lines.

Subject headings: stars: individual (BC UMa, SW UMa, BW Scl) – white dwarfs – novae, cataclysmic variables

1. Introduction

The study of accreting white dwarfs in close binaries is best accomplished using the far-ultraviolet (FUV) portion of the spectrum for systems with low mass transfer rates. In these cases, the peak flux of the 12 000–50 000 K white dwarf (Sion 1999; Gänsicke 2000) dominates the accretion disk. If the spectral resolution is on the order of 1 Å or better and the signal-to-noise ratio (S/N) at least of the order of 10, then the temperature, rotation rate and chemical abundances of the white dwarf can be determined reliably from a single FUV spectrum. This has been demonstrated within our past observations and analyses using the Space Telescope Imaging Spectrograph (STIS) for EK TrA (Gänsicke et al. 2001b), EG Cnc, HV Vir (Szkody et al. 2002c), LL And, EF Peg, (Howell et al. 2002), GW Lib (Szkody et al. 2002b), VY Aqr, WX Cet (Sion et al. 2003), and AL Com (Szkody et al. 2003b). The results of these past observations have shown that the coolest white dwarfs in disk-accreting systems cluster about 12 000–14 000 K, compared to single field white dwarfs, which have temperatures down to 5000 K. Thus, the white dwarfs in CVs are definitely heated by accretion (Sion 1995; Townsley & Bildsten 2003). However, it is clear that we do not yet fully understand the relation between close binary evolution, accretion heating and white dwarf cooling. The measured white dwarf temperatures do not monotonically decrease with decreasing orbital period, which would be expected in a simple picture where CVs evolve from long to short orbital periods and from high to low mass transfer rates (Howell et al. 2001). At least one additional parameter that determines the white dwarf temperatures in CVs are the white dwarf masses – which are poorly known. Furthermore, although several CVs are cool enough

to lie in the instability strip for pulsating ZZ Ceti white dwarfs (e.g. EG Cnc, Szkody et al. 2002c), only one of our STIS targets (GW Lib) is known to pulsate – and paradoxically, its white dwarf is apparently too hot to be a pulsator (Szkody et al. 2002b). Addressing the complex interplay between white dwarf properties and CV evolution clearly needs high-quality observational input for a sufficiently large sample of CV white dwarfs. In this paper, we present the analysis of the last three short-period dwarf novae from our Cycle 8 *HST*/STIS program displaying a white dwarf dominated far-ultraviolet spectrum: BW Scl, BC UMa and SW UMa.

BW Scl was initially found in the Hamburg/ESO quasar survey as HE 2350-3908 (Augusteijn & Wisotzki 1997) and independently discovered in the ROSAT survey as RX J2353.0-3852 (Abbott et al. 1997). Its extremely short orbital period (78.2 min), double-humped optical light curve (peak-to-peak variation 0.1 mag), spectrum with double-peaked Balmer emission flanked by broad absorption lines, and lack of visibility of any secondary star led Augusteijn & Wisotzki to conclude that this system was similar to WZ Sge a prototype of short period, low accretion-rate cataclysmic variables with extreme amplitude outbursts that only occur on time scales of tens of years. They used the X-ray flux to obtain a quiescent accretion rate of only $10^{-12}M_{\odot} \text{ yr}^{-1}$. To date, no outburst of BW Scl has been observed.

BC UMa was first identified as a large amplitude dwarf nova (Romano 1963). The first spectra by Mukai et al. (1990) revealed evidence of the white dwarf from absorption surrounding the emission lines, as well as a secondary star later than M5. They accomplished a crude fit to the blue spectrum and obtained a temperature of near 15 000 K and used the secondary to estimate a distance of 130–400 pc. Photometry by Howell et al. (1990) revealed *B* and *R* light curves with a single peak-to-peak variation of 0.25 mag at a period of 91 min when the system was at $V = 18.6$. Later photometry during quiescence and superoutburst (Patterson et al. 2003) showed a double-humped light curve with smaller amplitude when the system was at $V = 17.4$. They also refined the period from spectroscopy to 90.2 min.

SW UMa is also a large amplitude, short period dwarf nova, but which is known to have several types of outbursts (Howell et al. 1995). The first time-resolved study (Shafter et al. 1986) revealed an orbital period of 81.8 min from the spectra, while the photometry showed a repeatable 0.4 mag hump on most nights. But on one night, when the mean magnitude was about 0.5 mag fainter, the orbital variation disappeared and was replaced by a quasi-periodic oscillation with a period near 16 min. This change from hump presence to absence was also evident in the datasets of Howell & Szkody (1988). Another peculiarity of this system is the presence of a narrow $H\alpha$ emission component which is most prominent at orbital phase 0.3. Doppler tomograms constructed from several of the emission lines showed a prominent disk contribution in the optical with enhanced emission at phases 0.3, 0.6 and 0.9 (Szkody

et al. 2000). Thus, SW UMa appears to have a higher mass transfer rate and more extensive disk than BW Scl and BC UMa. Despite this, Gänsicke & Koester (1999) were able to see evidence of the white dwarf in the IUE spectra, and determined a temperature for the white dwarf of $16\,000 \pm 1500\text{K}$.

Our STIS spectra of these 3 systems are used to provide good constraints on the white dwarf temperature, disk contributions and variability of the UV compared to the optical light. Additionally, the good S/N for the brighter systems BC UMa and SW UMa allows us to obtain good values for the rotation rates and compositions of the white dwarfs.

2. Observations

2.1. BW Scl

BW Scl was observed in deep quiescence with *HST* during a single spacecraft orbit on 12 September 1999 (Table 1). From the STIS CCD acquisition image, we derive a $F28 \times 50\text{LP}$ magnitude of 16.5, roughly equivalent to an R band measurement. The data were obtained using the E140M echelle grating and the $0.2'' \times 0.2''$ aperture. The nominal spectral resolution of this setup is $R \sim 90000$, covering the range 1125–1710 Å. BW Scl was among the first targets observed in our Cycle 8 STIS program, and we opted for the echelle grating in order to accurately measure the rotational velocity of the white dwarf from the Doppler broadening of narrow metal lines. Unfortunately, the FUV flux of BW Scl was lower than expected, and the quality of the data is insufficient to exploit the high resolution of the E140M grating. Figure 1 shows the STIS data of BW Scl rebinned to a resolution of $\sim 250\text{ km s}^{-1}$. Clearly visible is the broad flux turn over at $\lambda \lesssim 1400\text{ Å}$ which we identify as the $\text{Ly}\alpha$ absorption line from the white dwarf photosphere. In addition, a large number of narrow metal absorption lines are detected, the most prominent ones being $\text{Si II } \lambda\lambda 1260,65$, a complex of C I lines near 1280 Å, the blend of $\text{Si II } \lambda\lambda 1304,05,09$ and $\text{O I } \lambda\lambda 1304,06$, $\text{C II } \lambda 1335$, a feature at 1432 Å which is most likely due to Ca II (possibly blended with some C I lines), $\text{Si II } \lambda\lambda 1527,33$, a blend of C I lines at 1556–58 Å, and $\text{Al II } \lambda 1670$. Broad $\text{Ly}\alpha$ and $\text{C IV } \lambda 1550$ emission are clearly present, the detection of narrow $\text{C III } \lambda 1176$ and $\text{He II } \lambda 1640$ emission is less secure. The quality of the data decreases towards the blue and red ends of the spectrum because of the decreasing response of the instrument. At the red end, the quality of the spectrum is deteriorated due to problems in extracting the individual echelle orders of this low-flux object, resulting in spurious emission/absorption edges. Finally, three small gaps between the echelle orders are present at 1653 Å, 1671 Å, and 1690 Å.

In order to extend the wavelength coverage of BW Scl for our analysis we have extracted

the optical spectrum presented by Abbott et al. (1997), renormalizing it to the average magnitude of the system, $V \simeq 16.4$ (Fig. 1). The broad Balmer absorption lines characteristic of a high-gravity white dwarf photosphere are clearly discerned.

2.2. BC UMa

BC UMa was observed with STIS for five consecutive spacecraft orbits on 2000 July 18 (Table 1). The last outburst of BC UMa previous to our STIS observations initiated on 2000 March 31, so the system had returned to its quiescent level long before the time of our HST pointing (Fig. 2). Analysis of the STIS acquisition image provides a F28×50LP magnitude of 18.4. After our experience with the use of the E140M grating for faint objects, we decided to use the G140L grating and the $52'' \times 0.2''$ aperture, providing a nominal resolution of $R \sim 300 \text{ km s}^{-1}$ over the wavelength range 1150–1715 Å. The STIS spectra of BC UMa obtained in the five individual *HST* orbits are nearly identical and have been co-added for the subsequent analysis (Fig. 1). As for BW Scl, the average STIS spectrum of BC UMa also clearly reveals the photospheric spectrum of the accreting white dwarf: a very broad Ly α profile superimposed by the same set of narrow low-ionization metal absorption lines. The only significant emission features are C III λ 1176, a broad Ly α (the narrow structures in Ly α are residuals from the not perfectly removed geocoronal airglow) and C IV λ 1550.

A single optical spectrum (red/blue pair) of BC UMa was obtained shortly before the *HST* pointing on 3 July 2000 using the Apache Point Observatory 3.5m telescope and Double Imaging Spectrograph with a $1.5''$ slit, giving $\sim 2.5 \text{ \AA}$ resolution spectra in the regions from 4200 – 5000 Å and 6300 – 7300 Å. The data were reduced and calibrated in a standard fashion using IRAF. The APO spectrum of BC UMa (Fig. 1) is very similar to that reported by Mukai et al. (1990), both in continuum flux and line strength. The weak H β to H γ emission lines are flanked by broad absorption troughs, which are presumably of white dwarf photospheric origin.

Additional optical spectroscopy of BC UMa was obtained at the MMT Observatory on the night of 29 March 2001 using the red channel spectrograph (Table 1). A total of 11 600s blue (4000–5250 Å) spectra and a single 600s red (5600–8500 Å) spectrum were obtained. The setup used a 1 arcsec slit giving spectral resolutions of 1 Å/pixel in the blue and 0.5 Å/pixel in the red. The night appeared to be nearly photometric and of constant ($\sim 1.2''$) seeing as evidenced by watching the slit viewer camera during the course of the observations. The data were reduced in IRAF using average bias and red/blue flat fields taken at the start of the night. The standard star Feige 34, used to flux the spectra, was observed near in time and airmass to the red spectrum and at the start of the blue time-series

sequence. The absolute flux calibration appears good to near 10% as estimated by using one standard star to flux another.

Figure 1 shows the average of the 11 blue spectra along with the single red spectrum. The emission lines are noticeably stronger and the overall flux level is higher in the MMT data, compared to the APO spectrum and to the spectrum in Mukai et al. (1990), suggesting that the MMT observations caught the system during a relatively active phase. The Balmer lines are double-peaked, suggestive of an origin from the accretion disk in a moderately high-inclination system. As noticed by Mukai et al. (1990), the secondary star is discerned in the red part of the spectrum. However, the quality of our single red spectrum is not sufficient to improve the spectral typing of Mukai et al. (1990).

2.3. SW UMa

SW UMa was observed with STIS during two consecutive space craft orbits on 2000 May 26 (Table 1). The data were obtained using the same instrumental setup as described in Sect. 2.2. The last outburst of SW UMa recorded before the STIS pointing started on 2000 February 12, lasted for ~ 20 d, and the system was in quiescence for ~ 85 d when the *HST* observations were carried out (Fig. 2). SW UMa was found at very similar flux levels during both *HST* orbits, and the average spectrum is shown in Fig. 1. Similar to BC UMa, the white dwarf in SW UMa is revealed through its broad Ly α absorption. However, in SW UMa the emission lines are much stronger compared to BC UMa. In addition to emission of C III,IV the STIS spectrum of SW UMa also contains emission of Si III λ 1206, N V λ 1240, Si IV λ 1393,1402, and He II λ 1640. The metallic absorption lines observed in BC UMa are overall weaker in SW UMa, possibly filled in by emission. Unambiguously detected in absorption are the C I complex at 1280 Å, the Si II/O I blend at 1300 Å, Ca II λ 1432, Si II $\lambda\lambda$ 1527,33, and Al II λ 1670.

SW UMa was observed on 2000 May 28 at the Apache Point Observatory. Similar to the ultraviolet wavelength range, the optical emission lines in SW UMa are also significantly stronger compared to BC UMa and BW Scl, suggesting a stronger contribution of the accretion disk. Correspondingly, the broad white dwarf photospheric absorption of H β and H γ is less pronounced in SW UMa than in BC UMa and BW Scl.

3. Spectral Analysis

Our approach in analyzing and modelling the STIS data of BW Scl, BC UMa and SW UMa is very similar to the methods described in detail in our earlier papers (e.g. Gänsicke

et al. 2001b; Szkody et al. 2002c; Howell et al. 2002). Here, we will only briefly summarise our general strategy.

At first, we derive the effective temperature T_{eff} of the white dwarf, as well as a rough estimate of the chemical abundances in the atmosphere. For this purpose, we use a grid of white dwarf models calculated using TLUSTY195 and SYNSPEC45 (Hubeny 1988; Hubeny & Lanz 1995), which covers $T_{\text{eff}} = 10\,000 - 25\,000$ K in steps of 100 K, $\log g = 7.0 - 10.0$ in steps of 0.1, and metal abundances of 0.1, 0.5, and 1.0 times their solar values. Whereas fitting model spectra to the observations of a single white dwarf allows a determination of T_{eff} as well as the surface gravity $\log g$, the success of this approach is very limited in the case of CV white dwarfs for two reasons: (1) the STIS FUV data, where the white dwarf is clearly the dominant emission component, do not provide sufficient wavelength coverage to break the degeneracy in T_{eff} and $\log g$. More specifically, only the red wing of Ly α is covered by the STIS observations; (2) in contrast to single white dwarfs where fitting the Balmer lines strongly constrains $T_{\text{eff}}/\log g$, the optical spectrum of CVs is severely contaminated by emission from the quiescent accretion disk. In the view of these limitations, we only use T_{eff} and the metal abundances as free parameters in the fit, keeping $\log g$ fixed. In order to account for the observed emission lines we fit the lines with Gaussian profiles, and we exclude the central 20 Å of Ly α from the fit to avoid contamination by residual geocoronal Ly α emission. The correlation between the assumed $\log g$ (= white dwarf mass) and the best-fit value for T_{eff} is then determined by repeating the fit while stepping through the grid in $\log g$. A nearly linear correlation between T_{eff} and $\log g$ is found (Fig. 3). Using a mass-radius relation for carbon-core white dwarfs (Hamada & Salpeter 1961) we obtain $M_{\text{wd}}(\log g)$ and $R_{\text{wd}}(\log g)$. The flux scaling factor between the white dwarf model and the STIS spectrum is then used to calculate the distance of the system, and the V_{wd} magnitude of the white dwarf is computed. M_{wd} , T_{eff} , d and V_{wd} are illustrated as a function of $\log g$ in the diagnostic diagrams shown in Fig. 3.

Once that T_{eff} is established, we refine the models in terms of the chemical abundances and white dwarf rotation rates. For each object, a grid of model spectra is generated (adopting the best-fit temperature for $\log g = 8.0$) that covers metal abundances from 0.1 to 1.0 times their solar values, in steps of 0.1, and rotation rates ($v \sin i$) ranging from 200 km s $^{-1}$ to 1000 km s $^{-1}$, in steps of 100 km s $^{-1}$. Several small wavelength ranges including metal lines of C, O, Si, and Al are then fitted, normalizing the model spectra to the local continuum (Fig. 4).

Additional details describing the analysis of the individual objects are given below.

3.1. BW Scl

The STIS spectrum of BW Scl is well described by a ($T_{\text{eff}} = 14\,800\text{ K}$, $\log g = 8.0$) model spectrum with 0.5 times solar metal abundances (Fig. 5, top-left panel). We find $\chi_{\text{red}}^2 = 0.8$, which implies statistically a very good fit. However, in view of the large errors of the echelle data (Fig. 5), a better statement is that our model is a good approximation considering the large uncertainties in the data. Extending the white dwarf model spectrum into the optical range does not provide much of a constraint on the white dwarf mass, as all models fall below the observed spectrum, as well as below the F28×50LP magnitude derived from the STIS acquisition image. Assuming a white dwarf mass in the range $0.35 - 0.90 M_{\odot}$ implies $T_{\text{eff}} = 14\,800 \pm 900\text{ K}$, and a distance of $d = 131 \pm 18\text{ pc}$.

Fixing $T_{\text{eff}} = 14\,800\text{ K}$ and $\log g = 8.0$, we determine $\simeq 0.5$ times solar abundances for carbon, oxygen and silicon, whereas aluminium is found to be significantly overabundant (by a factor three) with respect to its solar value (Fig. 4). We have investigated whether the effect of interstellar absorption could mimic the derived Al overabundance. Inspection of FUV interstellar absorption lines at both low and high galactic latitudes shows that the strength of Al II $\lambda 1670$ is comparable to that of Si II $\lambda 1260$, 1302 , 1527 , O I $\lambda 1302$, and C II $\lambda 1335$ (e.g. Lehner et al. 2001; Welsh et al. 2001). As we do not detect excess absorption in any of these other lines, we conclude that the observed enhancement of the Aluminium line is intrinsic to BW Scl, and suggests a substantial overabundance of Al in the photosphere of the white dwarf. The only caveat to this statement is that Al II $\lambda 1670$ is by far the strongest (factor ~ 10) Al line in the entire ultraviolet wavelength range. Confirming the Al abundance derived here would need high-resolution FUV (e.g. E140M) data at high S/N to make use of ~ 10 weaker Al II,III lines for spectral modelling. The narrow widths of the observed metal absorption lines implies a low rotation rate, $v \sin i < 300\text{ km s}^{-1}$.

3.2. BC UMa

Applying a simple white dwarf model fit to the STIS observations of BC UMa results in $T_{\text{eff}} = 15\,400\text{ K}$ for $\log g = 8.0$, however, this fit does not adequately reproduce the wavelength range $\simeq 1180 - 1250\text{ \AA}$, where the observed flux level significantly exceeds that of the model spectrum. In order to account for this additional component, we have repeated the fits to the STIS data of BC UMa, allowing for either a power-law or a blackbody contribution to the FUV spectrum. The best-fit parameter for the second component is either a power-law index of $\alpha = -0.04$ or a blackbody temperature of $14\,000\text{ K}$. In both cases, the additional continuum component contributes $\simeq 10\%$ of the flux at 1400 \AA . The white dwarf effective temperature remains nearly unchanged, $T_{\text{eff}} = 15\,200\text{ K}$, but the somewhat smaller scaling

factor results in a slightly larger distance estimate. Assuming again a white dwarf mass in the range $0.35 - 0.90 M_{\odot}$ we find $T_{\text{eff}} = 15\,200 \pm 1000$ K, and a distance of $d = 285 \pm 42$ pc.

Adding the second continuum component improves the fit in terms of χ_{red}^2 , which drops from $\simeq 3.4$ for the white-dwarf-only fit to $\simeq 2.2$ for the two-component models. On statistical grounds, both fits are poor, which is a sign that either the flux errors provided by the STIS pipeline are underestimated; there are additional systematic errors not accounted for by the pipeline; or that our model is not fully appropriate to describe the data. The reality is likely to be a mix of the second and third possibility. We have inspected high S/N STIS G140L spectra of the $\simeq 20\,000$ K single DA white dwarf GRW+70°5824 which reveal various wiggles that are not real and result in $\chi_{\text{red}}^2 > 1$ when fit with a model spectrum. In addition, our simple approach for approximating the disk emission by a component made up from a smooth slope plus Gaussian emission lines is certainly a fairly poor model for the reality. Keeping these limitations in mind, we adopted the following strategy to assess the statistical relevance of the second continuum component. We have renormalized the errors of the observed STIS spectrum so that $\chi_{\text{red}}^2 = 1$ for the two-component model. The wavelength independent factor used for this procedure was 1.45, which, assuming we had a perfect model for the data and no additional systematic errors, would imply that the flux errors provided by the pipeline are underestimated by this factor. Next, we calculated $\chi_{\text{red}}^2 \simeq 1420/903 \simeq 1.57$ for the single white dwarf fit using the renormalized errors, which implies that the single white dwarf fit is an unacceptable description of the data. On statistical grounds there is, however, no preference for either the white dwarf plus blackbody or white dwarf plus power law model: both two-component fits provide basically a nearly flat continuum component underlying the white dwarf emission, and improve the fit by similar amounts with respect to a single white dwarf model. The physical interpretation of the additional continuum component is emission either associated with the quiescent accretion disk or the hot spot. In the case of optically thin emission from an optically thin disk (or a thin hot layer on top of a colder optically thick disk), a power-law description would account for the wavelength dependence of the free-free absorption coefficient. Our blackbody approach would be a simple description for optically thick emission from the hot spot. At a distance of $d = 285$ pc, the radius of the blackbody component, assuming a spherical shape, would be $\simeq 2.9 \times 10^8$ cm. The temperature implied by the fit appears somewhat high with respect to the existing temperature estimates for hot spots (e.g. Panek & Holm 1984; Mateo & Szkody 1984; Szkody 1987), which are mostly based on blackbody analyses of either the orbital flux variation in the ultraviolet and/or optical or of the eclipse ingress/egress profiles. It is not too surprising that fitting a blackbody to the FUV continuum results in a different temperature estimate, moreover a blackbody is only a very simple approach. Extending the second component into the optical, it is clear that a simple power-law is an unphysical concept, as the free-free absorption coefficient breaks down

at the Balmer edge. In Fig. 5 we have plotted the UV-optical spectral energy distribution of BC UMa, along with the best-fit white dwarf plus blackbody model. Taking the flux level of the APO spectra at face value, they would constrain $\log g > 8.0$, i.e. $M_{\text{wd}} > 0.6 M_{\odot}$. However, the F28×50LP flux at the time of the *HST* observations exceeds that of the APO spectra, and we remain without a stringent constraint on the white dwarf mass. Real progress on the SED modelling of quiescent dwarf novae will need a realistic physical model for the emission of the accretion disk.

For the detailed metal line fitting, we fixed $T_{\text{eff}} = 15\,200$ K and $\log g = 8.0$, and find carbon, oxygen and silicon, abundances at 0.3 ± 0.1 times their solar values. As for BW Scl, the fit to Al II $\lambda 1670$ requires the abundance of aluminium to be significantly (by a factor two) super-solar. In contrast to the E140M echelle data of BW Scl, the G140L of BC UMa is not affected by instrumental features in the region around Al II $\lambda 1670$, lending further support for the detection of an enhanced Aluminium abundance. The observed line profiles are best fit with a rotation rate of $v \sin i = 300 \pm 100$ km s⁻¹.

3.3. SW UMa

In the case of SW UMa, the additional contribution in excess of the white dwarf photosphere is even more evident than in BC UMa. The emission lines of C III $\lambda 1176$, C IV $\lambda\lambda 1550$ and He II $\lambda 1640$ are much stronger, the emission lines of Si III $\lambda 1206$, N V $\lambda 1240$, C II $\lambda 1335$, Si IV $\lambda\lambda 1393, 1402$ are also clearly present, and the continuum flux underlying the white dwarf spectrum is substantially stronger.

Fitting the STIS spectrum with a white dwarf alone (plus Gaussian profiles for all the detected emission lines) results in $T_{\text{eff}} = 14\,700$ K for $\log g = 8.0$, but with a very high χ_{red}^2 of ~ 9.6 . Consequently, we applied the two-component model described in Sect. 3.2 to the STIS spectrum of SW UMa and find $T_{\text{eff}} = 13\,900$ K for the white dwarf (again for $\log g = 8.0$) plus a blackbody of $T = 17\,000$ K or a power law with a spectral index $\alpha = -0.04$ (Fig. 5). The non-white dwarf contribution to the continuum flux is $\simeq 20\%$ at 1400 Å. For a white dwarf mass in the range $0.35 - 0.90 M_{\odot}$, our fit to the STIS data implies $T_{\text{eff}} = 13\,900 \pm 900$ K and $d = 159 \pm 22$ pc. Adopting this two-component approach makes a substantial difference in χ_{red}^2 , which drops to $\simeq 2.4$ for both cases, white dwarf plus either a blackbody or a power law. The temperature of the blackbody component seems too high for a hot spot, but as mentioned above, a blackbody is probably an oversimplified model for the hot spot – if the hot spot is indeed the source of the observed additional continuum flux. For completeness the radius of the blackbody component, assuming spherical geometry and a distance of $d = 159$ pc, is 3.4×10^8 cm – very similar to that found in the case of BC UMa. For SW UMa, the optical

spectra do not provide an additional constraint on $\log g$, as all white models fall below the optical flux.

Fixing $T_{\text{eff}} = 13\,900\text{ K}$ and $\log g = 8.0$, we refined the analysis of the metal absorption lines, and find the abundances of carbon, oxygen and silicon to be at 0.3 ± 0.1 times their solar values. Similar to BW Scl and BC UMa, the abundance of aluminium is supra-solar by a factor 1.7. Some care has to be applied to these abundance measurements, as the presence of various strong emission lines could imply that the absorption lines observed in the STIS spectrum are filled in to some extent by emission. This should, however, not affect the large abundance ratio of aluminium to the other elements. It appears that the metal lines are not resolved at the resolution of the G140L grating, implying $v \sin i < 300\text{ km s}^{-1}$.

4. Short-term variability

All STIS data were obtained in the TIME-TAG mode, recording the arrival time and detector coordinate for each individual photon. This enables us to extract light curves over any selected wavelength range and at an arbitrary time resolution.

In the case of BW Scl, however, the use of the E140M echelle grating, which distributes the source photons over 44 individual echelle orders on the MAMA detector, prevents a reliable background subtraction. Extracting all photons and binning them into a 30sec light curve shows a low-amplitude modulation on a time scale of $\sim 30\text{ min}$. Alas, with the unknown contribution of the background, it is not possible to unequivocally ascribe this modulation to the source, or to the variation of the background throughout the orbit of *HST*. However, the STIS TIME-TAG data do not show any evidence for short-period flickering.

BC UMa was observed with the G140L first-order grating, and background-subtracted light curves were extracted for both the continuum and the C IV line (see Gänsicke et al. 2001a for a description of the methods used). Within the errors, the count rates are consistent with constant emission.

SW UMa was also been observed with the G140L grating, and we extracted continuum and C IV light curves (Fig. 6). Variability is seen on time scales ranging from $\sim 100\text{ sec}$ to $\sim 1500\text{ sec}$. A period (Lomb-Scargle) analysis of the data does not reveal any periodicities, specifically no signal is found either at the hypothetical 15.9 min white dwarf spin period (Shafter et al. 1986), or at the orbital period. The variance of the continuum and C IV light curves are 6% and 25%, respectively, clearly indicating that the flickering is primarily associated with the emission lines – in agreement with our results on EK TrA (Gänsicke et al. 2001b).

5. Discussion & Conclusions

As part of our medium-size Cycle 8 *HST*/STIS program, we have observed 16 cataclysmic variables, with the aim of significantly improving our knowledge about the properties of accreting white dwarfs in cataclysmic variables (Szkody et al. 2002d). For twelve systems, our strategy/selection worked well, and the analysis of the STIS spectra of their white dwarfs roughly doubled the number of effective temperature measurements for non-magnetic CV white dwarfs, and quadrupled the number of abundance/rotation rate estimates¹.

The white dwarf temperatures found range from $\simeq 12\,300$ K (EG Cnc, Szkody et al. 2002c) to $\simeq 18\,800$ K (EK TrA, Gänsicke et al. 2001b), with a strong clustering near $\simeq 15\,000$ K – where the three systems presented here also fall. In a simple-minded picture of CV evolution, one might expect the lowest white dwarf temperatures near the minimum period, where the accretion rates should be lowest. In our sample, this is not the case: BW Scl is the shortest-period ($P_{\text{orb}} = 78.2$ min) dwarf nova with $T_{\text{eff}} \simeq 14\,800$ K, whereas the coldest white dwarf ($T_{\text{eff}} \simeq 12\,300$ K) is found in EG Cnc at $P_{\text{orb}} = 86.4$ min. However, one significantly colder white dwarf has recently been found near the minimum period, HS2331+3905 ($P_{\text{orb}} = 81.1$ min, $T_{\text{eff}} \simeq 10\,500$ K; Araujo-Betancor et al. 2005), and some of the CV white dwarfs discovered by Sloan (Szkody et al. 2002a, 2003a) may turn out to be very cold as well. The observed spread in T_{eff} might to some extent be related to different white dwarf masses, as the accretion luminosity is, at constant accretion rate, proportional to $M_{\text{wd}}/R_{\text{wd}}$.

None of the 12 white dwarfs observed within our program is a rapid rotator – in fact, for most systems we could only determine upper limits on the rotation rate. This strongly suggests that the angular momentum coupling between the white dwarf envelope and its core is rather inefficient, and that the bulk of the accreted angular momentum is lost in the shell ejected during nova eruptions.

We have found substantial sub-solar abundances in all 12 white dwarfs analyzed in this program. It appears unlikely that these low white dwarf photospheric abundances reflect significant sub-solar metallicities of their donor stars, as the majority of CVs should be ordinary galactic disk objects. It is more likely that the abundances observed in the white dwarf photospheres reflect an accretion/diffusion equilibrium (radiative levitation is irrelevant for the low temperatures of most CV white dwarfs). While it would be of fundamental importance to estimate accretion rates from such equilibrium abundances, a quantitative ex-

¹The dwarf novae TY Psc, TZ Per were observed in outburst, DILac is an old nova where the white dwarf could not be detected (Moyer et al. 2003), and the analysis of the helium CV CP Eri is still in progress.

exploitation of this method is currently not possible as all published diffusion calculations have been carried out either for single DA or single DB white dwarfs, and we underline the need for detailed studies of diffusion time scales for various ions in CV white dwarf atmospheres. An additional uncertainty in the interpretation of the sub-solar abundances in CV white dwarfs is the uncertain distribution of the accreted material over the white dwarf surface, i.e. whether a lateral abundance gradient from the equator, where the material is accreted from the accretion disk, to the poles exist. While the current data can not be used to assess this possibility, future spectroscopy with high resolution and high S/N might shed light on this question, as the detailed shape of Doppler-broadened line profiles will depend on such a lateral abundance gradient.

Unfortunately, the low S/N prevented detailed abundance measurements of individual chemical species for most systems. The high S/N data presented here suggest an overabundance of aluminium in BW Scl, BC UMa, and SW UMa. At present, we are not yet able to interpret the abundance anomalies of some elements that have been observed in a number of CV white dwarfs in an unambiguous way. The peculiar abundances of odd-numbered nuclei may be related to proton-capture during classical nova eruptions, as suggested by Sion et al. (1997). Alternatively, abundance anomalies seen in the white dwarf atmosphere may just reflect abundance anomalies of the companion star as a result of its evolution in a binary system (Gänsicke et al. 2003; Harrison et al. 2004).

Our Cycle 8 program has quadrupled the number of reliable effective temperature measurements for short-period dwarf novae, and demonstrated the potential for abundance and rotation velocity measurements. Further progress in our understanding of both the properties of white dwarfs in CVs as well as CV evolution needs a larger sample of well-observed systems *and* a reliable estimate of their white dwarf masses – however, this progress crucially depends on the availability of FUV instruments with a higher throughput and higher spectral resolution, such as the Cosmic Origin Spectrograph could provide.

Acknowledgements

Based on observations made with the NASA/ESA Hubble Space Telescope, obtained at the Space Telescope Science Institute, which is operated by the Association of Universities for Research in Astronomy, Inc., under NASA contract NAS 5-26555. Part of the optical observations reported here were obtained at the MMT Observatory, a joint facility of the University of Arizona and the Smithsonian Institution. BTG was supported by a PPARC Advanced Fellowship. PS, EMS, and SBH acknowledge partial support of this research from HST grant GO-08103.03-97A. SBH acknowledges partial support of this work from

NSF grant AST 98-10770. An anonymous referee contributed a number of useful comments which helped to improve the paper.

REFERENCES

- Abbott, T. M. C., Fleming, T. A., & Pasquini, L. 1997, *A&A*, 318, 134
- Araujo-Betancor, S., Gänsicke, B. T., Hagen, H.-J., Marsh, T. R., Harlaftis, E. T., Thorstensen, J., Fried, R. E., Schmeer, P., & Engels, D. 2005, *A&A*, 430, 629
- Augusteijn, T. & Wisotzki, L. 1997, *A&A*, 324, L57
- Gänsicke, B. T. 2000, *Reviews of Modern Astronomy*, 13, 151
- Gänsicke, B. T. & Koester, D. 1999, *A&A*, 346, 151
- Gänsicke, B. T., Schmidt, G. D., Jordan, S., & Szkody, P. 2001a, *ApJ*, 555, 380
- Gänsicke, B. T., Szkody, P., de Martino, D., Beuermann, K., Long, K. S., Sion, E. M., Knigge, C., Marsh, T., & Hubeny, I. 2003, *ApJ*, 594, 443
- Gänsicke, B. T., Szkody, P., Sion, E. M., Hoard, D. W., Howell, S., Cheng, F. H., & Hubeny, I. 2001b, *A&A*, 374, 656
- Hamada, T. & Salpeter, E. E. 1961, *ApJ*, 134, 683
- Harrison, T. E., Osborne, H. L., & Howell, S. B. 2004, *AJ*, 127, 3493
- Howell, S. & Szkody, P. 1988, *PASP*, 100, 224
- Howell, S. B., Gänsicke, B. T., Szkody, P., & Sion, E. M. 2002, *ApJ*, 575, 419
- Howell, S. B., Nelson, L. A., & Rappaport, S. 2001, *ApJ*, 550, 897
- Howell, S. B., Szkody, P., Kreidl, T. J., Mason, K. O., & Puchnarewicz, E. M. 1990, *PASP*, 102, 758
- Howell, S. B., Szkody, P., Sonneborn, G., Fried, R., Mattei, J., Oliverson, R. J., Ingram, D., & Hurst, G. M. 1995, *ApJ*, 453, 454
- Hubeny, I. 1988, *Comput.,Phys.,Comm.*, 52, 103
- Hubeny, I. & Lanz, T. 1995, *ApJ*, 439, 875

- Lehner, N., Sembach, K. R., Dufton, P. L., Rolleston, W. R. J., & Keenan, F. P. 2001, *ApJ*, 551, 781
- Mateo, M. & Szkody, P. 1984, *AJ*, 89, 863
- Moyer, E., Sion, E. M., Szkody, P., Gänsicke, B., Howell, S., & Starrfield, S. 2003, *AJ*, 125, 288
- Mukai, K., Mason, K. O., Howell, S. B., Allington-Smith, J., Callanan, P. J., Charles, P. A., Hassall, B. J. M., Naylor, T., Smale, A. P., & Van Paradijs, J. 1990, *MNRAS*, 245, 385
- Panek, R. J. & Holm, A. V. 1984, *ApJ*, 277, 700
- Patterson, J., Thorstensen, J. R., Kemp, J., Skillman, D. R., Vanmunster, T., Harvey, D. A., Fried, R. A., Jensen, L., Cook, L. M., Rea, R., Monard, B., McCormick, J., Velthuis, F., Walker, S., Martin, B., Bolt, G., Pavlenko, E., O'Donoghue, D., Gunn, J., Novák, R., Masi, G., Garradd, G., Butterworth, N., Krajci, T., Foote, J., & Beshore, E. 2003, *PASP*, 115, 1308
- Romano, G. 1963, *Coelum*, 31, 1982
- Shafter, A. W., Szkody, P., & Thorstensen, J. R. 1986, *ApJ*, 308, 765
- Sion, E. M. 1995, *ApJ*, 438, 876
- . 1999, *PASP*, 111, 532
- Sion, E. M., Cheng, F. H., Sparks, W. M., Szkody, P., Huang, M., & Hubeny, I. 1997, *ApJ Lett.*, 480, L17
- Sion, E. M., Szkody, P., Cheng, F., Gänsicke, B. T., & Howell, S. B. 2003, *ApJ*, 583, 907
- Szkody, P. 1987, *AJ*, 94, 1055
- Szkody, P., Anderson, S. F., Agüeros, M., Covarrubias, R., Bentz, M., Hawley, S., Margon, B., Voges, W., Henden, A., Knapp, G. R., Vanden Berk, D. E., Rest, A., Miknaitis, G., Magnier, E., Brinkmann, J., Csabai, I., Harvanek, M., Hindsley, R., Hennessy, G., Ivezic, Z., Kleinman, S. J., Lamb, D. Q., Long, D., Newman, P. R., Neilsen, E. H., Nichol, R. C., Nitta, A., Schneider, D. P., Snedden, S. A., & York, D. G. 2002a, *AJ*, 123, 430
- Szkody, P., Desai, V., Burdullis, T., Hoard, D. W., Fried, R., Garnavich, P., & Gänsicke, B. 2000, *ApJ*, 540, 983

- Szkody, P., Fraser, O., Silvestri, N., Henden, A., Anderson, S. F., Frith, J., Lawton, B., Owens, E., Raymond, S., Schmidt, G., Wolfe, M., Bochanski, J., Covey, K., Harris, H., Hawley, S., Knapp, G. R., Margon, B., Voges, W., Walkowicz, L., Brinkmann, J., & Lamb, D. Q. 2003a, *AJ*, 126, 1499
- Szkody, P., Gänsicke, B. T., Howell, S. B., & Sion, E. M. 2002b, *ApJ Lett.*, 575, L79
- Szkody, P., Gänsicke, B. T., Sion, E. M., & Howell, S. B. 2002c, *ApJ*, 574, 950
- Szkody, P., Gänsicke, B. T., Sion, E. M., Howell, S. B., & Cheng, F. H. 2003b, *AJ*, 126, 1451
- Szkody, P., Sion, E., Gänsicke, B. T., & Howell, S. B. 2002d, in *The Physics of Cataclysmic Variables and Related Objects*, ed. B. T. Gänsicke, K. Beuermann, & K. Reinsch (ASP Conf. Ser. 261), 21–30
- Townsley, D. M. & Bildsten, L. 2003, *ApJ Lett.*, 596, L227
- Welsh, B. Y., Sfeir, D. M., Sallmen, S., & Lallement, R. 2001, *A&A*, 372, 516

Table 1. Log of the observations

Object	Telescope	Grating/ Resolution	Date UT	Magnitude	Exposure time [s]
BW Scl	HST	E140M	1999-09-12	16.5 ^a	1977s
	ESO 3.6m [†]	16 Å	1992-10-01	16.5 ^b	600 s
BC UMa	HST	G140L	2000-07-18	18.4 ^a	12998s
	APO	2.5 Å	2000-07-03	18.7 ^b	600s
	MMT	2.0 Å	2001-03-29	18.0 ^b	11 × 600 s
SW UMa	HST	G140L	2000-05-26	16.5 ^a	4933s
	APO	2.5 Å	2000-05-28	16.9 ^b	600s
^a F28x50LP	^b V	[†] from (Abbott et al. 1997)			

Table 2. Best-fit white dwarf parameter assuming $\log g = 8.0 \pm 0.5$

Object	T_{eff} [K]	$v \sin i$ [km s ⁻¹]	Metal Abundances (\odot)	d [pc]
BW Scl	14 800 ± 900	< 300	Al 3.0 ± 0.8, rest 0.5 ± 0.2	131 ± 18
BC UMa	15 200 ± 1000	300 ± 100	Al 2.0 ± 0.5, rest 0.3 ± 0.1	285 ± 42
SW UMa	13 900 ± 900	< 300	Al 1.7 ± 0.5, rest 0.2 ± 0.1	159 ± 22

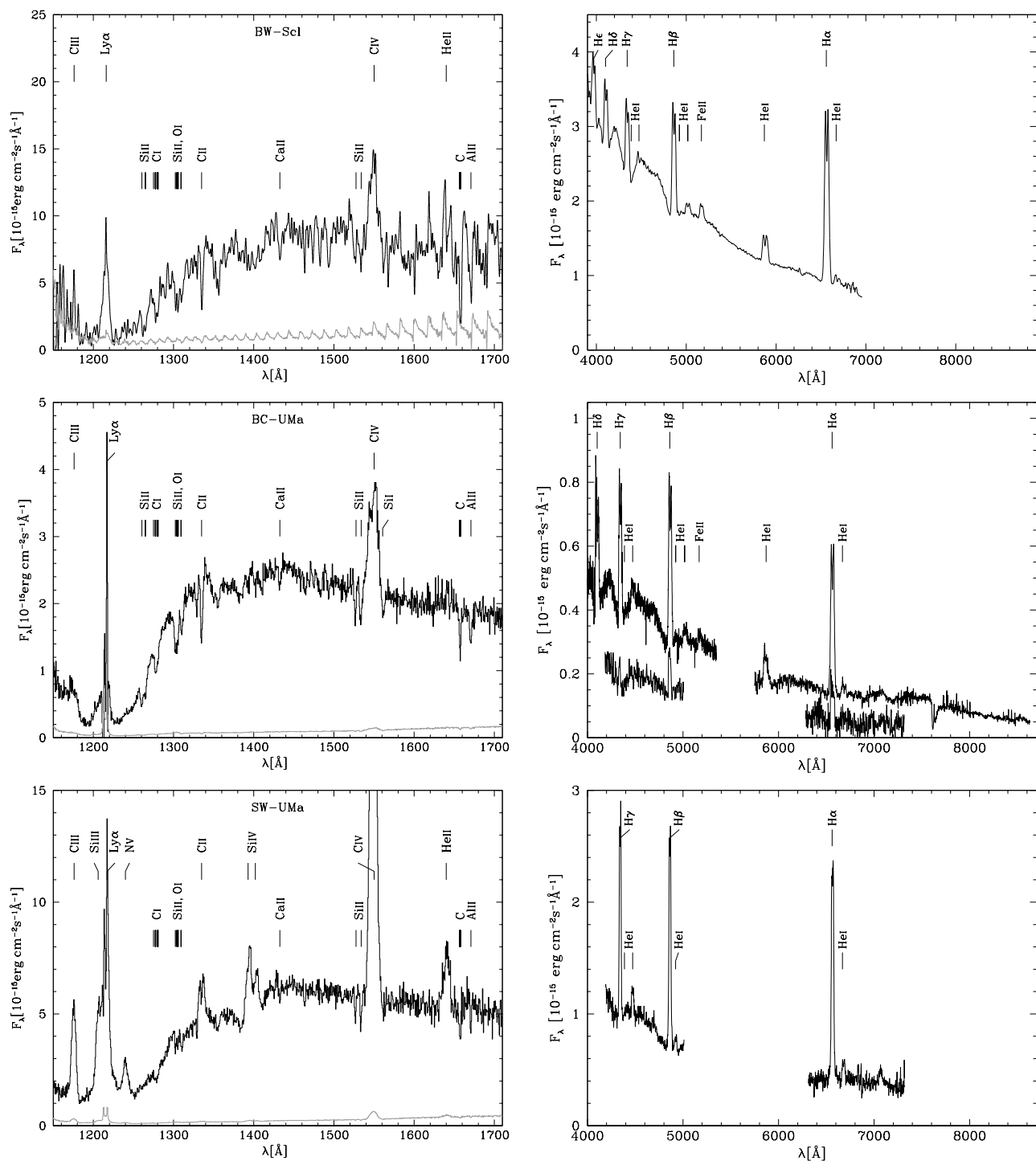


Fig. 1.— Average *HST*/*STIS* spectra of BW Scl (top), BC UMa (middle) and SW UMa (bottom). Prominent emission/absorption lines are identified. 1σ errors are shown in gray. BW Scl was observed with the E140M grating, the spectrum shown here has been convolved with a 0.6 \AA Gaussian. The S/N varies slightly over each individual echelle order.

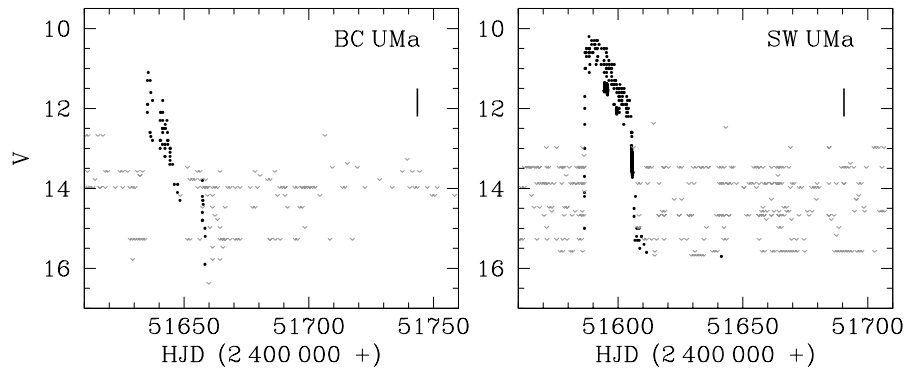


Fig. 2.— Excerpts from the AAVSO and VSNET optical long term light curves of BC UMa (left) and SW UMa (right) close to the *HST* observations. The dates of the *HST* observations are indicated by the tick marks.

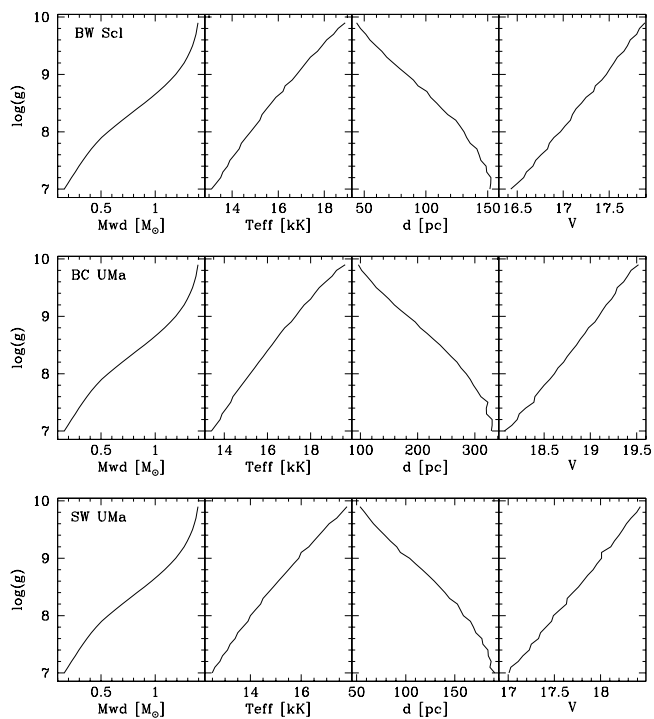


Fig. 3.— Diagnostic diagrams for the white dwarf model fits to the STIS data. The $\log g$ dependence was established by stepping through the the grid of fixed values for $\log g$, leaving the temperature and scaling factor free. For a given $\log g$ (or white dwarf mass), the solid lines indicate the effective temperature, distance, and V magnitude of the white dwarf implied by the fit.

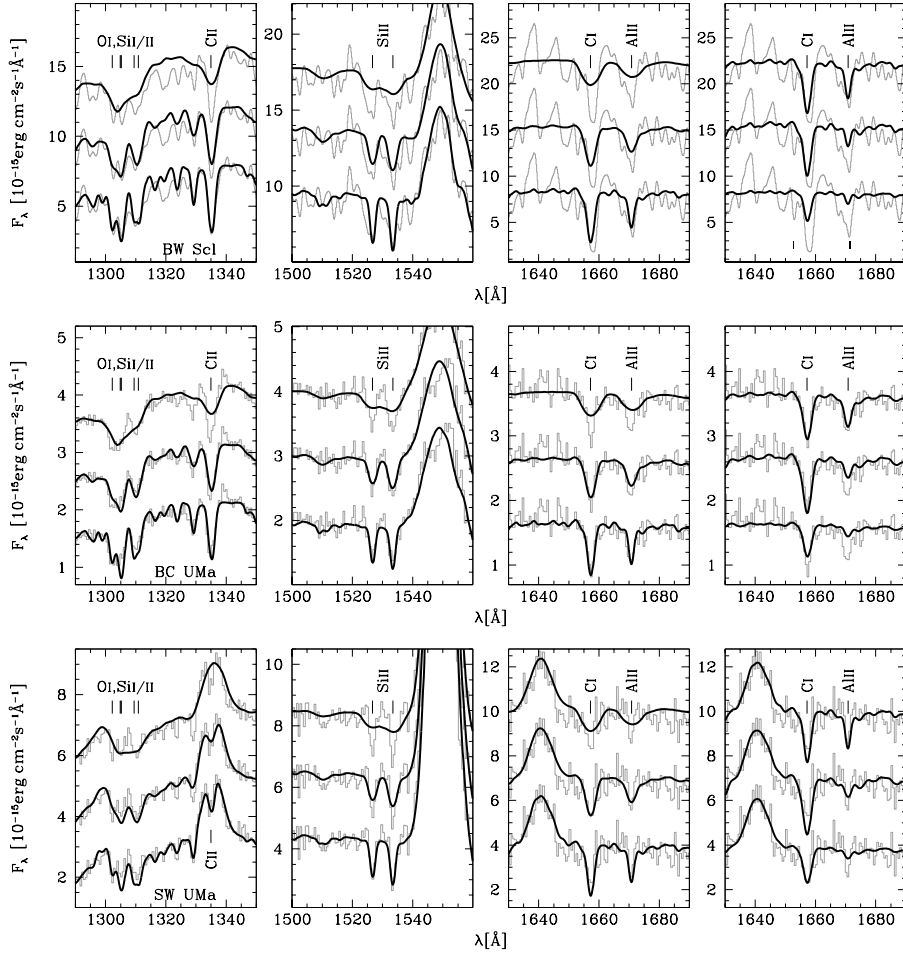


Fig. 4.— Detailed fits to the absorption lines of carbon, oxygen, silicon and aluminium. Top panels: BW Scl, all models have $T_{\text{eff}} = 14\,800$ K and $\log g$. The three left panels show the STIS data along with with white dwarf model spectra for $0.5\times$ solar abundances and rotation rates of 200 km s^{-1} (bottom curve), 400 km s^{-1} (middle curve) and 800 km s^{-1} (top curve). The right panel shows models for a rotation rate of 200 km s^{-1} and $0.1\times$ solar abundances (bottom), $0.7\times$ solar abundances (middle) and $0.3\times$ solar abundances for all metals except $3.0\times$ solar abundances for aluminium. Middle panels: equivalent plots for BC UMa, with $T_{\text{eff}} = 15\,100$ K and $\log g = 8.0$. The abundances are $0.3\times$ solar in the left panels where varies from $v \sin i = 200, 400, 800\text{ km s}^{-1}$. In the right panel, $v \sin i = 300\text{ km s}^{-1}$, but $0.1\times$ solar abundances in the bottom curve, $0.6\times$ solar in the middle curve. The top curve has $0.3\times$ solar for all metals except aluminium, which has $2.0\times$ solar abundances. Bottom panels: equivalent plots for SW UMa, with $T_{\text{eff}} = 13\,900$ K and $\log g = 8.0$. The metal abundances in the left panels are $0.2\times$ solar their values, and $v \sin i = 200, 400, 800\text{ km s}^{-1}$. The right panel shows $v \sin i = 300\text{ km s}^{-1}$, and $0.1\times$ solar abundances (bottom curve) and $0.5\times$ solar abundances (middle curve). The top curve shows all metals at $0.2\times$ solar abundances, except aluminium at $1.7\times$ its solar value

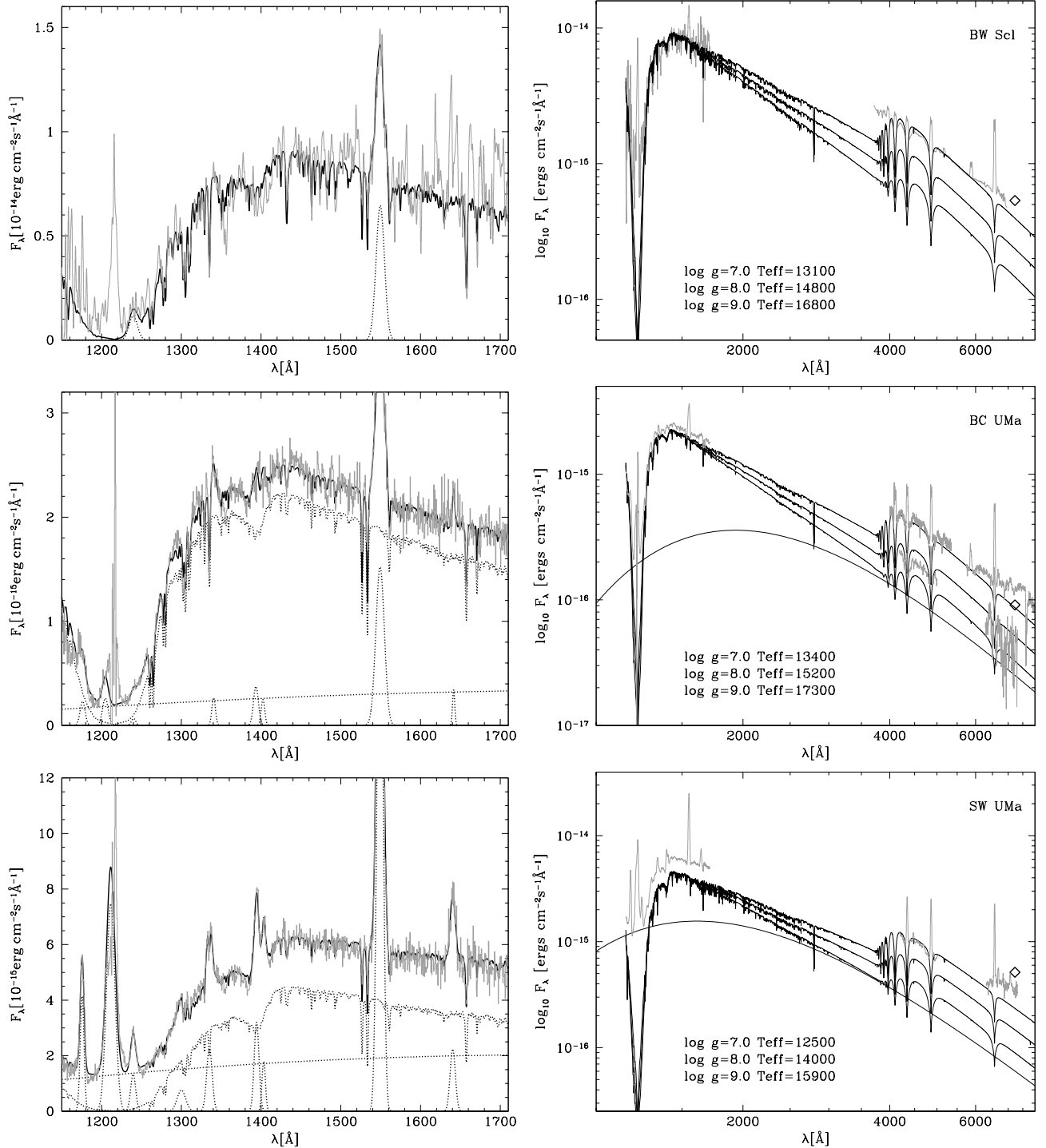


Fig. 5.— Model fits to the STIS spectra. From top to bottom: BW Scl, BC UMa, SW UMa. Left panels: the STIS wavelength range. For BW Scl, we fitted the STIS data with a white dwarf model spectrum plus Gaussian emission lines. BC UMa and SW UMa were modelled with a white dwarf plus blackbody for the continuum, plus Gaussian emission lines. Right panel: Extrapolation of the models into the optical wavelength range. The observed spectra are shown in gray. The F28×50LP fluxes determined from the STIS acquisition images are indicated by the open diamonds.

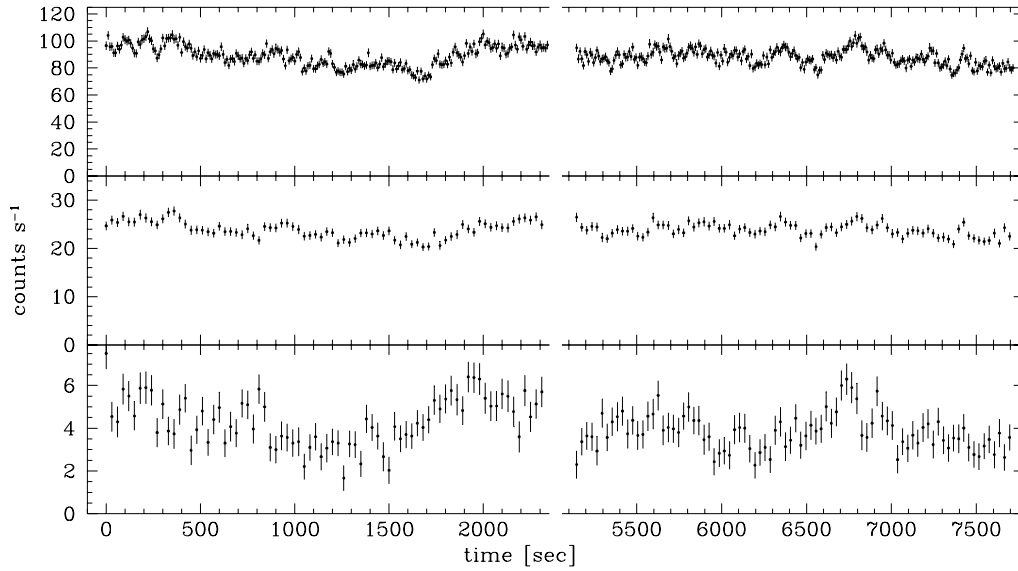


Fig. 6.— The far-ultraviolet light curves of SW UMa extracted from the STIS TIME-TAG data. Top panel: 1230 – 1710 Å, 10 s time resolution. Middle panel: line-free continuum, 1420 – 1520 Å, 30 s time resolution. Bottom panel: C iv line, 30 s time resolution.